Experimental Methods and Imaging for Enzymatically Induced Calcite Precipitation in a micro-fluidic cell

Felix Weinhardt[1], Holger Class[2], Samaneh Vahid Dastjerdi[3], Nikolaos K. Karadimitriou[1], Dongwon Lee[3], and Holger Steeb[1]

[1]University of Stuttgart
[2]Institut for Hydraulic Engineering
[3]University of Stuttgart, Institute of Applied Mechanics (CE)

November 24, 2022

Abstract

Enzymatically Induced Calcite Precipitation (EICP) in porous media can be used as an engineering option to achieve targeted precipitation in the pore space, e.g. with the aim to seal flow paths. This is accomplished through an alteration of porosity and, consequently, permeability. A major source of uncertainty in modelling EICP is in the quantitative description of permeability alteration due to precipitation. This study investigates experimentally the time-resolved effects of growing precipitates on porosity and permeability on the pore scale in a PDMS-based micro-fluidic flow cell. The experimental methods are explained; these include the design and construction of the micro-fluidic cells, the preparation and usage of the chemical solutions, including the injection strategy, and the monitoring of pressure drops at given flux rates to conclude on permeability. Imaging methods are explained with application to EICP, including optical microscopy and X-Ray micro-Computed Tomography (XRCT) and the corresponding image processing and analysis. We present and discuss detailed experimental results for one particular micro-fluidic set-up as well as the general perspectives for further experimental and numerical simulation studies on induced calcite precipitation. The results of the study show the enormous benefits and insights of combining both light microscopy and XRCT with hydraulic measurements in micro-fluidic devices. This allows for a quantitative analysis of the evolution of precipitates with respect to their size and shape, while monitoring the influence on permeability. We can demonstrate that we improved the interpretation of monitored flow data dependent on changes in pore morphology.

Experimental Methods and Imaging for Enzymatically Induced Calcite Precipitation in a micro-fluidic cell

Felix Weinhardt[1], Holger Class[1], Samaneh Vahid Dastjerdi[2], Nikolaos Karadimitriou[2], Dongwon Lee[2], Holger Steeb[2,3]

[1]Department of Hydromechanics and Modelling of Hydrosystems, University of Stuttgart, Pfaffenwaldring 61, 70569 Stuttgart, Germany
[2]Institute of Applied Mechanics, University of Stuttgart,Pfaffenwaldring 7, 70569 Stuttgart, Germany
[3]SC SimTech, University of Stuttgart,Pfaffenwaldring 7, 70569 Stuttgart, Germany

Key Points:

- An experimental set-up for reliable pressure measurement in micro-fluidic cells with continuous enzyme-induced calcite precipitation
- Synchronizing time-resolved optical microscopy with pressure measurements allows for correlating pore space alteration with permeability
- X-Ray micro-Computed Tomography complements optical microscopy for estimating volume changes from 2D projections of the precipitates

Corresponding author: Felix Weinhardt, `felix.weinhardt@iws.uni-stuttgart.de`

Abstract

Enzymatically Induced Calcite Precipitation (EICP) in porous media can be used as an engineering option to achieve targeted precipitation in the pore space, e.g. with the aim to seal flow paths. This is accomplished through an alteration of porosity and, consequently, permeability. A major source of uncertainty in modelling EICP is in the quantitative description of permeability alteration due to precipitation. This study investigates experimentally the time-resolved effects of growing precipitates on porosity and permeability on the pore scale in a PDMS-based micro-fluidic flow cell. The experimental methods are explained; these include the design and construction of the micro-fluidic cells, the preparation and usage of the chemical solutions, including the injection strategy, and the monitoring of pressure drops at given flux rates to conclude on permeability. Imaging methods are explained with application to EICP, including optical microscopy and X-Ray micro-Computed Tomography (XRCT) and the corresponding image processing and analysis.

We present and discuss detailed experimental results for one particular micro-fluidic set-up as well as the general perspectives for further experimental and numerical simulation studies on induced calcite precipitation. The results of the study show the enormous benefits and insights of combining both light microscopy and XRCT with hydraulic measurements in micro-fluidic devices. This allows for a quantitative analysis of the evolution of precipitates with respect to their size and shape, while monitoring the influence on permeability. We can demonstrate that we improved the interpretation of monitored flow data dependent on changes in pore morphology.

1 Introduction

Induced calcite precipitation is an engineering option which could be employed for a targeted sealing of flow paths in the subsurface as it might be necessary in geological gas storage in the presence of conductive faults (Phillips, Lauchnor, et al., 2013; Phillips, Gerlach, et al., 2013; Ebigbo et al., 2010; Hommel et al., 2013), for creating barriers for groundwater and containment of subsurface contamination (Cuthbert et al., 2013), for soil stabilization and for an improvement of mechanical soil properties (Wiffin et al., 2007; van Paassen et al., 2010; Hamdan & Kavazanjian, 2016). There are different techniques to achieve a targeted calcite precipitation at a desired location. One of them is referred to as Enzymatically Induced Calcite Precipitation (EICP). Basically, EICP as we employ it here, relies on the dissociation of urea into carbon dioxide and ammonium catalyzed by the enzyme urease which is extracted from jack-bean meal. In circum neutral environments regarding the pH value, ammonium ($NH_4{}^+$) and bicarbonate are the dominant products of hydrolysis, see Eq. (1) (Mitchell et al., 2019). However, carbon dioxide in aqueous solutions occurs as carbonic acid (H_2CO_3), bicarbonate ($HCO_3{}^-$) or carbonate ($CO_3{}^{2-}$), depending on the pH value. Since ammonia acts as a weak base by taking up a proton and producing hydroxide, it increases the pH value and shifts the equilibrium towards carbonate ions. The additional presence of calcium ions, in our case provided by adding calcium chloride, forces calcium carbonate to precipitate. According to van Paassen (2009), the release of a proton (H^+) during the calcium carbonate precipitation buffers the production of hydroxide during the hydrolysis, see Eq. (2). Precipitated calcium carbonate eventually results on the pore scale in a change in pore morphology and on a larger scale, after averaging, in a change of the effective quantities porosity and permeability,

$$\mathrm{CO(NH_2)_2} + 2\,\mathrm{H_2O} \xrightarrow{\text{urease}} 2\,\mathrm{NH_4{}^+} + \mathrm{HCO_3{}^-} + \mathrm{OH^-}, \tag{1}$$

$$\mathrm{HCO_3{}^-} + \mathrm{Ca^{2+}} \longrightarrow \mathrm{CaCO_3}\downarrow + \mathrm{H^+}. \tag{2}$$

A more commonly known method, Microbially Induced Calcite Precipitation (MICP) relies on microbes expressing the enzyme urease. While the basic mechanism of precipitating carbonates altering the pore morphology is similar as in EICP, the MICP technology is more complex in application; and in particular, the impacts on porous-media properties are even more challenging to model. MICP involves the growth of bacteria and biofilms that have also an influence on the evolving pore space, however not the same as the precipitated calcite. Biofilm is a soft matter and to some extent flexible to adapt to variable shear stress at variable flow velocity. In contrast, precipitated carbonates tend to be more rigid solids.

Models for MICP have focused recently on the reaction part and its kinetics (Bachmeier et al., 2012; Ebigbo et al., 2010; Hommel et al., 2015), but kinetics are often strongly coupled to hydraulic processes (Ebigbo et al., 2012; Hommel et al., 2016). While it has been shown that MICP models can be successfully applied to field-scale application (Cunningham et al., 2019; Minto et al., 2019), it is extremely challenging to describe quantitatively the impact of combined biofilm growth and carbonate precipitation on porosity and permeability, since the two "solid" phases have totally different properties (Hommel et al., 2018).

In this study, we aim at elaborating much-needed experimental evidence for a more thorough knowledge on the relation between altered pore morphology and the larger scale model parameters permeability and porosity. We acknowledge that the Darcy scale (or REV scale), see e.g. the respective definitions in Hommel et al. (2018), is the appropriate scale to model field-scale applications of MICP or EICP, where computational demands can become a limiting factor. However, it is the pore scale where the morphological changes occur and from where we, consequently, need to derive new insights. Therefore, we aim at studying the processes on this scale, and we use micro-fluidics for analyzing them in the details of our interest.

Precipitation processes in micro-fluidic devices have been studied in the past with various objectives. In the work of Zhang et al. (2010), mixing-induced carbonate precipitation was investigated in a micro-fluidic cell made out of Pyrex glass and silicon with the dimensions of 2 cm x 1 cm. The process was observed by optical microscopy with a resolution of 1.62 and 0.65 μm/pixel. Yoon et al. (2012) performed pore-scale simulations based on these experiments. Wang et al. (2019) studied MICP in a micro-fluidic chip made out of Poly-Di-Methyl-Siloxane (PDMS) with the dimension of 1.5 $cm\times$1.5 cm, fabricated very similar compared to the one that is used here. With a very high resolution of 0.65 μm/pixel, they were able to observe bacteria, as well as to capture qualitatively the shape of single crystals. In contrast, the experiments of Kim et al. (2020) were performed on a larger scale, observing the whole micro-fluidic chip over time with a resolution of 6.5 μm/pixel, during sequential injections of reactive solutions for EICP. The micro-fluidic chip was made out of glass and has the dimensions of 2.1 $\times$ 1.3 cm. Based on image processing, statistical analysis of the precipitates, more precisely the size distribution over time, were conducted and compared to a simplified kinetic model.

For our study, we hypothesize that the growth of biofilm has completely different impact on flow resistance on the pore scale than precipitated carbonates. Eventually, this holds then also in terms of effective permeability on the Darcy scale. Therefore, this study is exclusively focusing on EICP in a micro-fluidic cell; this reduces the complexity compared with MICP since biofilm growth is not occurring. An important question that we want to address in our micro-fluidic experiments is the issue of where nucleation and crystal growth occurs, and whether precipitation in pore cavities or pore throats is more relevant for reduction of permeability and improvement of soil stability, the latter is not in the focus of this study. By an analysis of nucleation and crystal growth on the pore scale we pursue the vision to derive substantial new insights in porosity-permeability relations, which then need to be upscaled to the Darcy scale. Precipitation inside a porous medium is a complex process influenced by different chemical and physical phenomena. Besides the hydrolysis of urea, the precipitation itself is a complex combination of nu-

cleation, crystal growth, and changes of crystal structure (van Paassen, 2009). Six different polymorphs of calcium carbonate exist: calcite, aragonite, vaterite, mono-hydrocalcite, ikaite and amorphous calcium carbonate (ACC), where the thermodynamical stablility decreases from calcite to ACC (El-Sheikh et al., 2013). Especially when there is homogeneous nucleation, we have to keep in mind that crystals can form, dissolve and recrystallize into another polymorph which is well studied in the work of Kralj et al. (1990, 1994, 1997). Homogeneous nucleation takes place when small nuclei form in a pure liquid phase, while heterogeneous nucleation defines the crystallization at the interface of another phase, which could be, for example, dust or an other existing nucleus (Nebel, 2008).

As already mentioned above, it is very important to get reliable quantitative information on the change of pore volume, i.e. porosity on the Darcy scale, and on the alteration of pore morphology. The micro-fluidic cells we use here have a very small depth compared to the other two dimensions. Optical microscopy and image processing can provide mainly 2D information with limited details in the through-plane direction. As a complement to optical microscopy, X-Ray micro-Computed Tomography (XRCT) was used to acquire information also in the through-plane direction. Our primary focus is on the change in the hydraulic parameters, like permeability, due to the growth of precipitates. Therefore, it is necessary to monitor the pressure reliably. The experiments presented here combine the visual observation of crystal nucleation and growth over time with reliable pressure measurements under continuous flow conditions. We use a time-consuming XRCT analysis of the form and shape of the crystals in order to develop cheaper methods for interpreting microscopy-based 2D information which still can consider typical 3D morphology of precipitated carbonates. This will allow more comprehensive studies on EICP, and perspectively also on MICP, and its particularly complex porosity-permeability relations.

Furthermore, the results presented here can serve as a basis for a comparison study of reactive transport simulations on the pore scale, including calcite precipitation.

Below, we introduce the materials and methods that are used, developed, and applied. This includes the production of the micro-fluidic cells by soft lithography, the experimental procedures for the EICP studies, as well as the imaging techniques. Subsequently, we present results on permeability determination from exemplary experiments. The discussion of the results puts a focus on the development of methods and a workflow that is appropriate for the EICP application. Still, we are able to draw important conclusions for further studies towards a better understanding of porosity-permeability relations in porous media affected by EICP or MICP.

2 Materials and methods

The set-up and the workflow of the micro-fluidic experiment, including the preparation of the chemical solutions are described in detail below. Subsequently, the two imaging methods, optical microscopy and XRCT-scanning, are described and the corresponding post-processing of the images is explained.

2.1 Micro-fluidic experiments

In the scope of this work, three experiments were conducted, in the following referred to as Experiments 1, 2, 3. For each experiment, one micro-fluidic cell was produced, based on the same design. Also the set-up, experimental procedure and image processing were mainly the same and are explained in the following, while minor differences are pointed out.

The micro-fluidic cells were produced by following the regular workflow of soft lithography (Karadimitriou et al., 2013; Xia & Whitesides, 1998). The designs of the pore-network geometry were generated with AutoCAD© and subsequently printed on a A4 transparency, with the pore space being transparent and the solid space being opaque. Such a transparency is commonly called as a mask. These masks are employed in optical lithography with the use of SU8-2100 photoresist to produce photo-resist spin-coated silicon wafers. After having followed the regular steps of photo-lithography, the photo-resist features sticking out of the wafer had a height of 85 μm. These wafers were used in the production process of the actual micro-fluidic cells out of Poly-Di-Methyl-Siloxane (PDMS). A mixture of Dow Corning SYLGARD© 184 Silicone Elastomer base and the curing agent, at a mixing ratio of 10:1, is poured into a petri dish with a wafer, so as to create the PDMS slab with the features of the flow network. An equal quantity of the mixture is also poured into another petri dish without a wafer, to create a blank slab which is used as the sealing one. After degassing and subsequent curing for 2 hours at 68 °C, the resulting PDMS slides are carefully removed from the wafer and the petri dish. Holes (ø1.5 mm) for the inlet and outlet tubes are punched and the PDMS slides are diced to fit the size of a standard glass slide for microscopy (26 mm×76 mm). The bonding of the two PDMS slabs together and subsequently on a glass slide is done with the corona treatment described in Haubert et al. (2006). After another 24 hours, the bonding is complete and the micro-fluidic cells are ready to be used in the experiments.

The reactive solutions were prepared in the following way: Solution 1 contained 1 g urea with a molar mass of 60.06 $^{g}/_{mol}$ and 2.45 g calcium chloride dihydrate with a molar mass of 129 $^{g}/_{mol}$ mixed in 50 ml deionized water. The mass concentrations correspond to a equimolar concentration of 1/3 $^{mol}/_{L}$. Both chemicals were provided by MERCK©. For Solution 2, the enzyme urease is extracted from jack-bean meal (JBM) provided by Sigma Aldrich©. 0.25 g jack-bean meal together with 50 ml water are stirred at a constant temperature of 8 °C. After 17 hours of stirring the solution is vaccuum filtered twice with a 0.45 μm cellulose membrane to remove any JBM particles remaining. In Table 1, the concentrations of the reactive solutions are summarized.

Table 1. Concentrations of the solutions

Solution	Urea $[^{mol}/_{L}]$	Calcium chloride $[^{mol}/_{L}]$	JBM $[^{g}/_{L}]$
Solution 1	0.33	0.33	-
Solution 2	-	-	5
Mixed	0.167	0.167	2.5

The design of the micro-fluidic cell and its geometrical parameters are shown in Figure 1. The inlet at the bottom left is connected with two 2.5 ml glass syringes (S_1, S_2) guided by two, one for each, mid pressure pumps CETONI neMESYS 100N which generate the flow. The interface between the syringe pumps and the computer is the base module, CETONI BASE 120. The software QMixElements is used to operate the experiment via pre-defined scripts. The tubes, connecting the micro-fluidic cell with the syringes and the pressure sensors have an inner diameter of 0.5 mm and an outer diameter of 1.59 mm (1/16 inch) and are made of Teflon (Poly-Tetra-Fluoro-Ethylene, PTFE). The outlet is connected to a reservoir with a constant water table of 10 cm above the micro-fluidic cell. This induces a back-pressure in order to reduce the risk of bubble formation during the experiment. Air bubbles can lead to difficulties in image post-processing, as shown in the work of Kim et al. (2020), and are likely to disturb the pressure measurements. The tubes for the outlet have an inner diameter of 0.75 mm to avoid clogging. P_1 and P_2 indicate the location of the Elveflow MPS0 pressure sensors with a range

of 70 mbar. The analog voltage signals of the pressure sensors are acquired and digitized with 16 bit using the CETONI I/O module at a rate of 1 Hz. The design of the micro-fluidic cell shows features of the porous domain which are smaller than the inlet and outlet geometry. The pressure sensors are connected in parallel to the inlet channel and outlet, and this offers the ability to measure pressures under static conditions. The inlet channels are large enough to be hydraulically connected to the pressure sensor during the whole precipitation process. Thus, it is possible to measure the pressure drop of the domain of interest (top right in Figure 1) without being compromised by precipitates in the inlet and outlet channels of the micro-fluidic cell. The porous domain in this work is defined as shown in Figure 1 on the right. Note that we define here permeability being specific for this particular porous domain. The domain is a cuboid with dimensions $D_{pore} \times H \times L_{domain}$. Permeability is later on used in absolute values; therefore, a reference domain is required. For porosity, we are detaching this from permeability since we are only interested later on in changes of void space due to precipitation. We will then use the notation of a "normalized porosity".

Each experiment can be subdivided into three stages: a) initial permeability measurement, b) continuous injection of reactive solution, and c) final permeability measurement. The ambient temperature was 23 °C.

In the beginning of the experiment the permeability is estimated by applying different flow rates (0.01 - 1.5 μL/s) with de-ionized water only, and measuring the pressure difference $\Delta p = p_2 - p_1$. Based on these measurements, the initial permeability of the porous domain can then be determined using Darcy's Law (Stage a). Afterwards, the micro-fluidic cell is flushed with both reactant solutions at a high flow rate of 0.25 μL/s for 5 minutes. Urea-calcium-chloride solution is introduced from S_1 and urease solution from S_2, in order to fully saturate the micro-fluidic cell with the reactive solution. Consequently, the continuous injection of reactive solution starts: a constant flow rate of 0.01 μL/s for each syringe is applied for up to 5 hours, resulting in a total flow of 0.02 μL/s and a forced mixing of the reactants in the inlet tube right before the micro-fluidic cell (Stage b). During this stage, precipitation is taking place and the pressure is continuously monitored at the inlet and outlet of the micro-fluidic cell in order to quantify the hydraulic effects of the pore space alterations. After precipitation, the system is flushed with water at a constant flow rate of 0.02 μL/s for 20 minutes. Finally, another permeability estimation is conducted by applying flow rates from 0.005 to 0.03 μL/s with water only (Stage c).

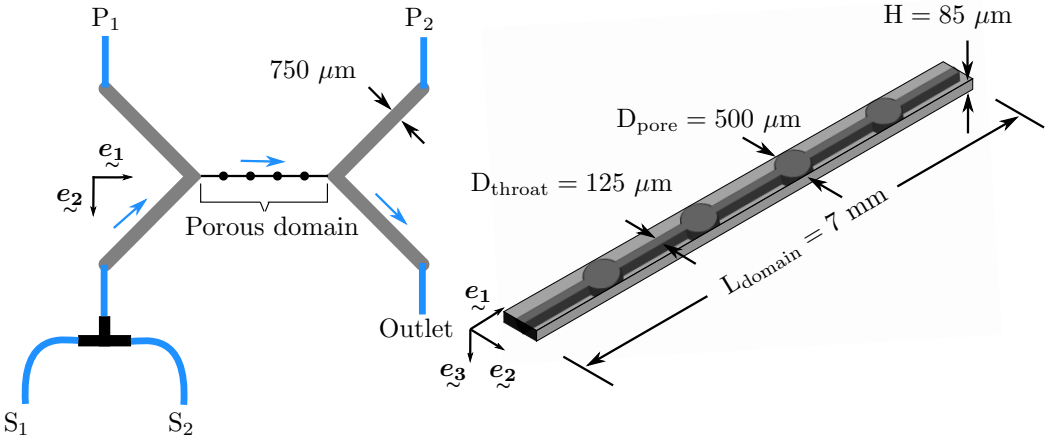

Figure 1. Left: sketch of the micro-fluidic set-up including the porous domain (black), the inlet-, outlet- and pressure- channels (gray), the tubes (blue) connected to the syringe pumps (S_1 and S_2) and to the pressure sensors (P_1 and P_2), the flux is indicated with blue arrows; right: porous domain and its dimensions

2.2 Imaging

During the experiments, the processes were observed through optical microscopy, while in addition the micro-fluidic cells underwent an XRCT scan after the experiment. The set-up and the subsequent image processing of these methods are detailed in the following.

2.2.1 Optical microscopy

The transparent nature of PDMS allows for the direct visualization of the processes taking place in the pore space, in real time, by using transmitted light microscopy. For this purpose, a custom-made microscope has been developed, which is able to visualize samples with a resolution of 0.5 to 20 μm per camera pixel. In the Supporting Information a sketch with all components is given. An extended version of this optical set-up can be found in Karadimitriou et al. (2012).

During the precipitation phase of the Experiments 1 and 2, images were captured at 0.1 fps at a resolution of 3.34 and 3.36 μm/pixel respectively. Experiment 3 was observed at 1 fps with a resolution of 3.17 μm. In order to analyze the images with respect to the porosity change and the crystal growth, the gray scale images were processed using the software Matlab R2019b (The Mathworks, Inc.) using a procedure as explained in the following. As a first step, a mask was created that defines the porous domain based on the initial image without any precipitates. For creating the mask, at first the anisotropic diffusion filter is applied (Perona & Malik, 1990). Consequently, the image is binarized and the regions outside of the porous domain are filled (*imfill*). The morphological closing operation (*imclose*) is used to remove impurities of the image. Since the raw image also includes parts outside of the domain of interest and is not perfectly parallel to the e_1 axis, the image is cropped and rotated in order to be horizontally aligned. This results in a binarized image where the void space is defined as 1 and the solid as 0 (Figure 2 a). The mask obtained so far serves then as a reference for future identification of the crystals in the same domain.

When comparing images at different time steps while precipitation is still taking place, it is important that they are geometrically aligned. Even though the set-up, including the stage and the camera, are fixed, small changes of the position can occur. To overcome this issue, all subsequent images are registered to the initial image. Matlab's intensity-based image-registration function *imregister* is used with the transformation type rigid. This only allows for rotation and translation by bi-linear interpolation. Once the images are registered, the porous domain can be extracted by applying the same geometrical operation as for creating the mask. Since these images have the same size as the mask a subsequent element-wise multiplication with the mask is used to extract the void space of the cell. In order to remove the noise of the images while preserving the sharpness of edges, an anisotropic diffusion filter is applied (Perona & Malik, 1990). Consequently, the images are binarized using Otsu's method (Otsu, 1979). Since the void space has the value of 1 and the solid (including the precipitates) has the value of 0, a 2D-porosity can be estimated by calculating the mean of the binarized images. A flow chart in the Supporting Information shows the different image processing steps.

Figure 2 shows the different steps of the procedure. In order to study the crystal aggregates individually, the Matlab-function *bwlabel* is used to identify connected objects in the binary image. Subsequently, the area of these objects is determined with the function *regionprops*. Based on this area, which can be seen as a 2D projection of the crystal aggregates, a corresponding volume is estimated. In Section 3.3, this is explained and investigated in detail.

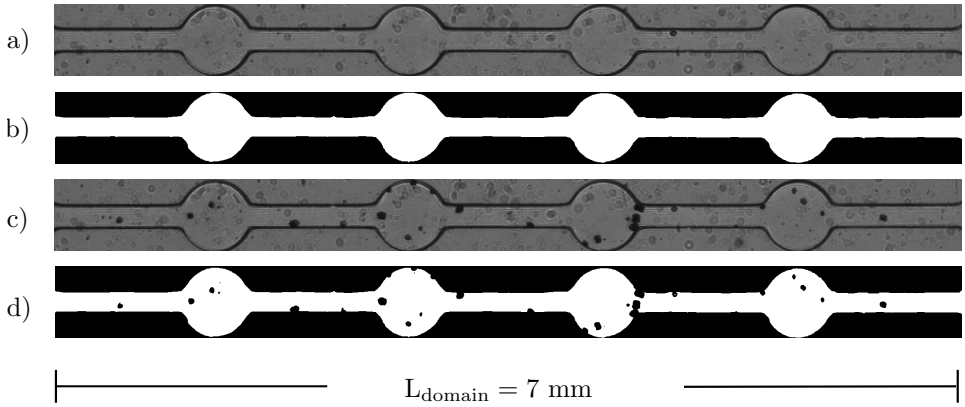

Figure 2. Image processing procedure for optical microscopy: a) initial image b) mask c) raw image with precipitates d) processed image with precipitates

2.2.2 X-Ray micro-Computed Tomography (XRCT)

After the EICP experiment, the micro-fluidic cells were further investigated by means of XRCT imaging. The scan was performed in open and modular XRCT device which was set-up during the last years. More details about the set-up can be found in the work of Ruf and Steeb (2020) or in the Supporting Information. The micro-fluidic cell domain was cut out from the total 3D scanned volume. With the resolution of 4.25 $\mu m/px$, the size of the XRCT-imaged area (after alignment) is 2100 × 519 × 20 voxels in length, width and depth of the porous domain respectively, This corresponds to a domain volume of approximately 89 mm × 22 mm × 0.085 mm.

XRCT-scanning was carried out for all three experiments 1-3. However, due to the vast amount of a second phase around the precipitates after the experiments and before the scans, which will be explained in 3.2.2, only the XRCT data set of Experiment 3 was further post-processed.

Image processing was performed again by using Matlab R2019b (The Mathworks, Inc.). The raw images were imported to Matlab as a 3D data set. To carry out the statistical study and ease the comparison to the 2D information, the images were transformed to achieve a 3D dataset, in which the porous domain is aligned as it is in the microscopy images. See Figure 3 (a) for an example of the 3D data set. Afterwards the images were filtered with a 3D median filter with a kernel size of [3 3 3] and segmented. Two methods, (i) of maximum entropy and (ii) Otsu (Otsu, 1979) thresholding were applied to segment the images into 4 different phases, including the PDMS, the pore space, the calcium carbonate precipitates, and a liquid-resembling phase surrounding some of the crystals (Figure 3 (b)). To detect the precipitates and in an effort to create a binarized mask for separating the precipitates from the sides of the channel, without loosing any volume of the precipitates, they were flagged with the value of 1, while the rest of the domain was flagged with the value of 0. A projection of all of the slides on the x-y plane was produced and the pixels not belonging to the crystals were removed. This mask was then multiplied by the 20 images to obtain the crystals. A more detailed descrition of the mask and its preparation can be found in SI. Upon that, the single crystals were detected using the Matlab-function *bwconncomp*, which returns the connected components found in the binary volume. The particles smaller than 10 voxels, which are mostly noise, were removed from the 3D precipitates with the function *bwareaopen*. The remaining connected components, referred to as crystals, were then investigated.

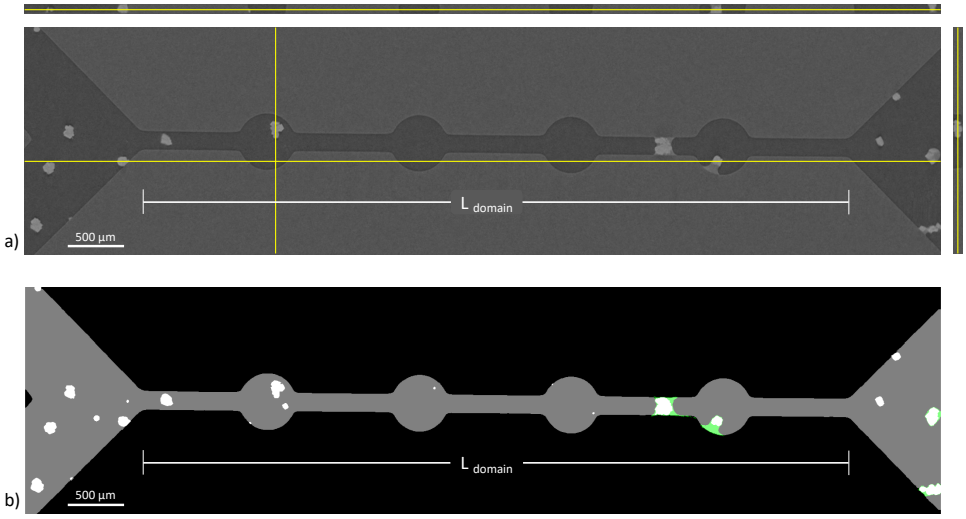

Figure 3. Image processing procedure for XRCT a) sections of the 3D data set b) projection of the segmented volume in the planar view (black: the PDMS, gray: the void space, white: the crystals, green: the second phase)

3 Results

We present and discuss here the results of the three experiments with the methods described in the previous sections. At first, we describe the estimation of the permeability by evaluating the pressure measurements in comparison to the applied boundary flow conditions. Subsequently, the precipitates are characterized by analyzing both the data gained from optical microscopy and the data obtained by XRCT.

3.1 Determination of Permeability

The permeability of the cell which is free from precipitates, and this with precipitates was estimated applying various boundary flow rates of de-ionized water and measuring the corresponding pressure drop (Stage a and c). By rearranging Darcy's Law and using the slope of the negative pressure drop over the flow rate s_{pq}, the intrinsic permeability k can then be calculated as:

$$k = \frac{\mu\, L_{domain}}{A\, s_{pq}}\,, \tag{3}$$

with A being the cross-sectional area ($H \times D_{pore}$) and L_{domain} the length of the domain as defined in Figure 1. For example, Figure 4 displays the measured negative pressure drop over the flow rate for Experiment 1. The applied flow rates in the case of the clean cells (before precipitation) have a wider range (up to 1.5 $^{\mu\mathrm{L}}/_{\mathrm{s}}$) in order to overcome the relatively large error for small pressure drops. In the case of the cells having precipitates, the permeability is expected to be significantly reduced, inducing higher pressure drops for the same boundary flow conditions. This allowed us to employ lower flow rates in our effort to avoid detachment of the precipitates due to increased shear stresses, while still being able to measure the corresponding pressures in a reliable way. The calculated permeabilities of the three experiments are summarized in Table 2.

The boundary pressure is monitored continuously during the entire injection and precipitation period (Stage b). Under the reasonable assumption that the fluid viscos-

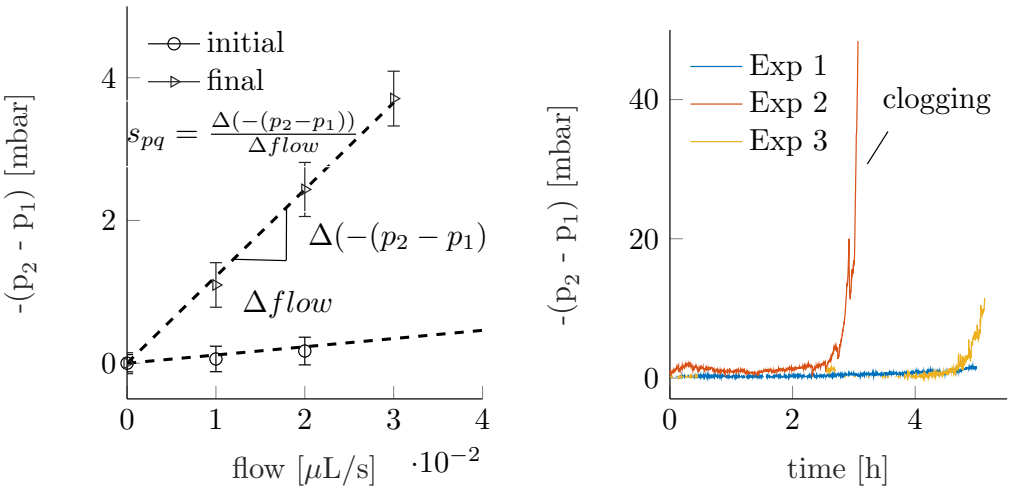

Figure 4. Left: negative pressure drop over flow rate for the cell at initial state and at the final state, after the precipitation - exemplary for experiment 1; the slope s_{pq} is used to estimate the permeability based on equation (3); right: negative pressure drop during the precipitation phase of Experiment 1, 2, and 3.

Table 2. Permeability of initial state (k_0) and after the precipitation (k_{prec})

Experiment	k_0 $[10^{-10}\mathrm{m}^2]$	k_{prec} $[10^{-11}\mathrm{m}^2]$	k_{prec}/k_0 [−]	log10(k_{prec}/k_0) [−]
1	1.43 ± 0.04	1.35 ± 0.14	0.095	-1.02
2	1.36 ± 0.10	< 0.005	< 0.00036	< -3.42
3	1.39 ± 0.08	0.23 ± 0.12	0.016	-1.79

ity remains constant throughout the duration of the experiment, the normalized permeability is the reciprocal of the normalized pressure drop ($k/k_0 = \Delta p_0/\Delta p$). Figure 4 shows the negative pressure drop of Experiments 1, 2, and 3 during the precipitation process. While Experiment 1 shows a slow and steady increase of the pressure drop for the 5 hours of injection, Experiments 2 and 3 show a stronger increase at certain times. The pressure drop of Experiment 2 rises sharply after 2.5 hours of injection. Since the monitored pressure was close to the pressure range of the sensor, the injection had to be stopped. Even at a reduced flow rate of 0.002 μL/s the pressure reached the limit instantaneously. This corresponds to a permeability reduction of more than three orders of magnitude. In contrast, the pressure drop observed in Experiment 3 remained low over a period of about 4 hours. Since the pressure drop in this period was very small, minor fluctuations potentially caused by small leakages or bubbles in the system led to pressure drops below zero, which was the case for the period between 0.5 and 3 hours of injection. However, the pressure drop started rising after approximately 4 hours and the pressure measurement is therefore less sensitive to small imperfections of the set-up. The experiment was stopped after 5 hours and 5 minutes in order to prevent complete clogging as we saw it in Experiment 2. The precipitates caused a total permeability reduction of 1.69 orders of magnitude. For both Experiment 1 and Experiment 3, the permeability reductions obtained from the subsequent permeability measurement (Stage c) were slightly higher compared to the last measurement during the continuous injection. We think the reason for this is the following. The solution with reactants in the inlet tube has to be

flushed through the micro-fluidic cell before being able to continue with injecting water at different flow rates. This may result in further ongoing precipitation. Since the micro-fluidic cell from Experiment 2 was apparently clogged, the subsequent permeability measurement could not be performed. However, since we determine the initial and final permeability by injection of water at different flow rates, we are confident that this allows us to verify the continuous pressure measurement during the precipitation phase. This experimental protocol demonstrates that the continuous pressure monitoring strategy as explained here leads to reliable results for the obtained permeability reductions of up to three orders of magnitude.

3.2 Characterization of the precipitates

In the following section three additional steps for characterizing the precipitates are described. At first, based on the images obtained from optical microscopy the evolution of the pore morphology is investigated. Secondly, the final state of the Experiment 3 is additionally examined by means of the XRCT data set with a focus on the shape of the crystal aggregates. In the last step, an appropriate approach is presented that aims at allowing quantification of the volume of single crystal aggregates only based on their 2D projection. The results of optical microscopy are complemented based on this approach to estimate the volume of the precipitates over time since XRCT presently only gives us the final result of precipitation. In combination with the continuous pressure measurements, the permeability change is correlated to the change of porosity.

3.2.1 Evolution over time as derived from optical microscopy

We can see from the three experiments presented here that the complexity of the precipitation processes can lead to very different results in terms of where and how many nuclei form, even though the boundary conditions are kept the same. Figure 5 shows the final images of the three experiments. Since Experiment 2 was stopped after 3 hours, the states of Experiments 1 and 3 are also shown at that time for comparative purposes. The difference with the final state for each experiment is colored in gray.

The position of the nucleation sites do not seem to be influenced by the geometry. More precisely: we cannot conclude whether they are preferably located in the pore bodies or in the pore throats. The nuclei seem to be spread randomly throughout the domain, but they could be influenced by small imperfections of the micro-fluidic cell itself. For example, small impurities of the elastomer base or curing agent originated during the manufacturing process of the micro-fluidic cells might cause these imperfections which can result locally in an increased roughness of the surface. These imperfections can then act as initiation points and are therefore a preferred location for heterogeneous nucleation. Most of the crystals stay at the same position throughout the whole injection and grow continuously, which has also been observed during a sequential injection of reactive solutions in the work of Kim et al. (2020).

Figure 6 shows the 2D porosity normalized to the initial value over time. In Section 2.2, the procedure of obtaining the 2D porosity is explained. Experiments 1 and 2 show a similar trend of the reduction of the porosity over time, while in Experiment 3 the apparent pore volume decrease is slower. As Figure 5 shows, in Experiment 3 there are clearly less nuclei in the porous domain. This lack of nucleation sites leads to a smaller decrease of the apparent 2D porosity over time.

In addition to the average change of the pore volume over time, the growth of crystal aggregates can individually be observed in detail. Figure 6 shows a close-up of Experiment 2, where gray indicates the growth of the crystals during 1 hour and 40 minutes of injection. Based on a qualitative observation, two distinct phenomena can be clearly observed: a) the crystals mainly grow into the upstream direction of the flow, and b) the crystals in the pore throats grow faster compared to the ones in the pore bodies. For now, these are qualitative observations and need to be studied and verified in more detail. Re-

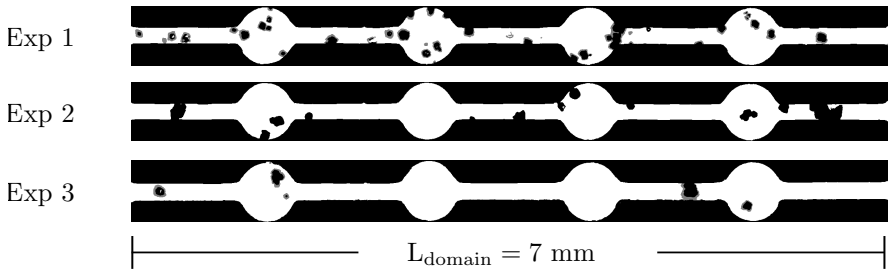

Figure 5. Processed images from optical microscopy of Experiments 1, 2, and 3. Black indicates the crystals after 3 hours and 10 minutes. Gray indicates the further development until the final states for Experiments 1 and 3

active transport models on the pore scale that include crystal growth could support this investigation (personal communication, not yet published).

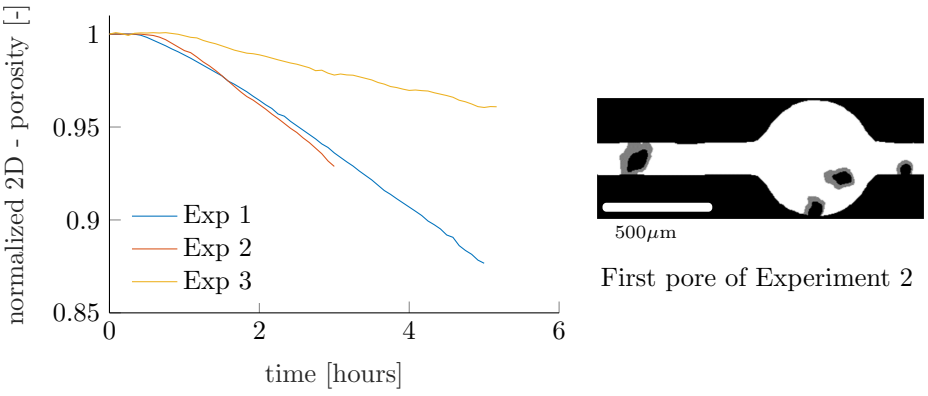

Figure 6. Left: normalized 2D porosity over time; right: crystal growth in the first pore of Experiment 2; gray indicates the growth within a period of 100 minutes

Figure 7 shows a time series of three unprocessed images from Experiment 2. Even though the solid crystals mainly stayed at their initial position, we observed also a case where an aggregate of crystals moved during the injection. The circle highlights the crystal that changed its position. Once it got stuck between two other crystals they continued to grow. Additionally, smaller grayish crystals can be seen around the darker and larger crystals. These could be meta stable polymorphs of calcium carbonate conglomerating close to the darker crystalline phase. The grayish crystals are apparently more likely to be transported with the flow. This can lead to a sudden clogging at locations where the cross-sectional area is already reduced. This is the case in the pore throat shown on the three images on the right in Figure 7. Here, the darker crystals narrow the cross-sectional area, and the grayish crystals are transported through it. As a consequence, pressure builds up during temporary plugging and subsequently relieves when the smaller crystals are pushed through. The alternating pressure buildups and relieves can be mainly seen for Experiment 2 in Figure 4 at a time where the domain is close to complete clogging. This again shows the enormous benefit of combining continuous pressure measurements with optical microscopy.

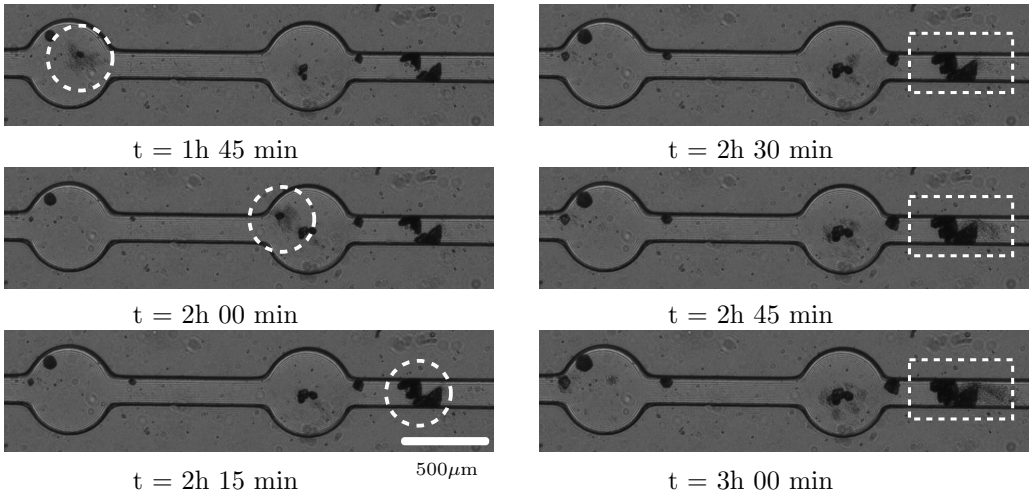

Figure 7. Time series of unprocessed images from optical microscopy of Experiment 2: a crystal moved to another location (indicated with the circle); accumulation of smaller grayish crystals in the pore throat (indicated with the rectangle)

3.2.2 Final state as derived from XRCT-scan

In order to examine the shape of the crystal aggregates, the XRCT-images are segmented and studied following the procedure as described in Section 2.2.2.

One of the advantages of 3D imaging in this study is the possibility it offers to define the volume of the precipitates accurately, since this allows for a reliable estimation of the porosity change in the 3D porous domain.

Moreover, the individual crystals are examined with respect to finding the best assumption for the shape of the crystals from the 2D images. Even though the area of interest for the determination of permeability in the experiments is the actual porous domain, the investigations of the XRCT-data are carried out on the total scanned domain, which includes other parts of the cell as well. The investigation, with the focus being mainly on the shape-defining properties of the crystals, includes their volume, surface, and their distribution in the cell's depth (top, bottom, side or the whole depth). Given that the main purpose of performing a XRCT is to enhance the microscopy imaging with 3D information, the ideal case would be to preserve the final state of the crystals at the end of the experiments as accurately as possible. Despite of the measures we took to ensure that preservation, such as rinsing and drying the cell after the experiment, it is observed in this study that there is a second phase surrounding some of the crystals. This phase has different X-Ray attenuation properties, leading to distinctly different intensities of the gray values in the acquired images (Figure 8 (a)). This occurrence can also be spotted by comparing two microscopy images, from which one is taken at the end of the experiments and the other is from before running the XRCT (Figure 8 (b) and (c)), although the dissimilarity in the two mentioned phases is not conspicuous. The discrepancy between the acquired information motivates detailed evaluation of the mentioned crystals in order to serve the purpose of the study, which is to support the 2D images from microscopy with the 3D images from XRCT.

Another observation is that all of the crystals with the mentioned phenomenon are located downstream of the crystal shown in Figure 9 (c), which should be taken into account, when trying to understand the nature of the second phase. The combination of the crystals and the second phase around them encapsulates a uniform distribution in the depth of the channel from which more than 50% of the volume is the second phase. It is notable that the mentioned phase demonstrates the properties of a saline liquid. Fig-

ure 8 (d) illustrates the classification of the two phases based on the difference in the gray values from the 3D imaging.

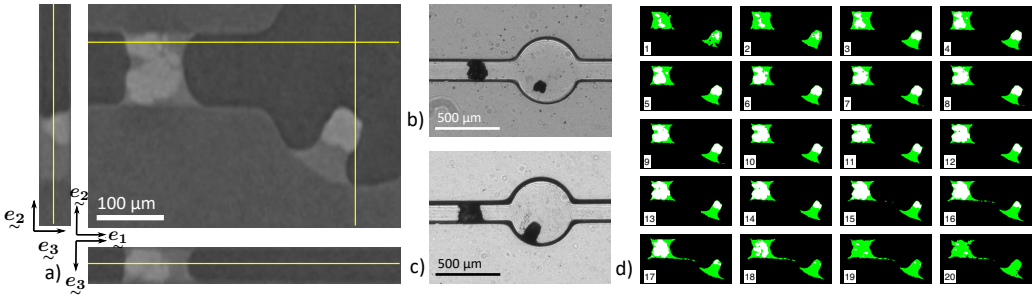

Figure 8. Two of the crystals, which have a second phase around them a) sections of the crystals from XRCT, b) microscopy image at the end of the experiment, c) microscopy image before the XRCT, d) classification of the precipitates into main crystal (white) and the second phase surrounding them (green) in the depth of the cell.

We should state that in an attempt to be more compatible with the microscopy images, the second phase is removed from the XRCT dataset and the investigations are carried out on the resulting dataset. Another information that can be derived from XRCT is the surface of the channel, where the crystals are attached to. This provides clues about where they started growing and can be of importance since it is not obtainable from the microscopy imaging effortlessly. An evaluation of the crystals' attachment locations shows that the number of the crystals attached to the top or sides of the channel is higher than the ones attached to the bottom surface. Out of the 21 crystals, 9 are extended in the whole depth of the cell, 7 are attached to the top, 3 to the sides and 2 to the bottom. Apart from the crystals which are connected only to the top surface of the cell, 7 out of 9 crystals which are extended in the whole depth of the channel have bigger attachment surfaces at the top. This claims that the nucleation probably started at the top. Based on these results obtained from image analysis, we can speculate that the surface roughness plays a significant role in the nucleation process in the current set-up. We reach to this conclusion based on the production process of the micro-fluidic cell, since the bottom surface is initially in contact with the surface of the petri-dish, and is expected to show a decreased roughness in comparison to the other surfaces forming a closed channel in the cell and are molded in contact with the wafer surface.

The third advantage of the 3D imaging in this study is the opportunity it offers to determine the distribution of the aggregates in the depth of the cell, which leads to a better estimation of the crystal shapes and volume. Four examples of the crystal voxels distribution in the depth of the cell are shown in Figure 9. In Figure 9 (a), a small crystal is shown which has grown on the side of the porous domain. In the bar chart the distribution of the crystal voxels, representing the volume of the crystal, is illustrated. It can be observed that the crystal is extended from the 8^{th} voxel in the depth to the 16^{th}. Figure 9 (b) shows a crystal which has grown through the whole depth and is showing a bigger surface on the top of the cell. The significantly larger amount of the voxels in the middle of the depth in the channel, where the flow velocity is at its most, is interesting. The crystal in Figure 9 (c) is one of the few which entraps a second phase around it and its extents has reached the walls of the porous domain at top, bottom and sides. Although the number of the voxels in the depth demonstrates an almost uniform distribution, after the classification of the two phases it can be seen that the distribution of the main crystal illustrates a pattern in the depth with the biggest area in the middle of the cell, which is similar to the crystals without the second phase around them. In contrast, the second phase is observed to be neighboring the sides of the cell, which

can be because of the wetting properties of the cell material toward trapped chemicals and reinforces the speculation that the second phase is a liquid. The crystal in Figure 9 (d) is one of the two crystals which has grown at the bottom of the cell. Its bigger area around the middle of the channel is similar to many of the other crystals.

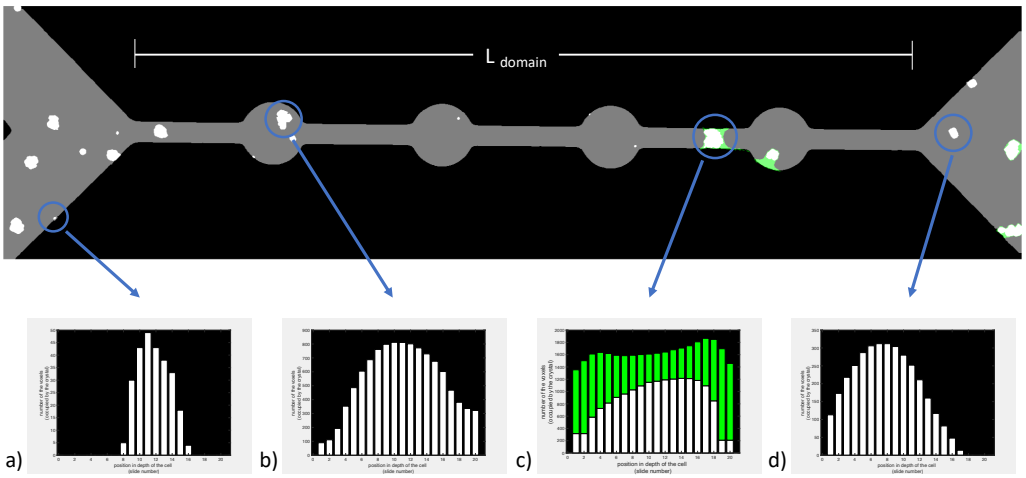

Figure 9. Examples of the distribution of the crystals in depth of the cell a) a crystal attached to the sides of the cell b) a crystal occupying the whole depth of the cell c) a crystal (white) with a second phase (green) around it d) a crystal attached to the bottom of the cell.

3.3 Complementing the 2D imaging with 3D information

From 2D microscopy, we can easily observe crystal growth over time. However, the actual volume change including the third dimension can only be derived with further assumptions. In the work of Kim et al. (2020), the volume of individual crystals is estimated by assuming the shape of the crystals to be either cylindrical or semi-spherical. From the area observed by optical microscopy (A), an equivalent radius (r_{eq}) is calculated:

$$r_{eq} = \sqrt{\frac{A}{\pi}}. \tag{4}$$

The volume of individual crystals is then estimated based on the equivalent radius and the height of the micro-fluidic cell, H (equations 5a and 5b). However, in the work of Kim et al. (2020), the shapes are just hypothetical and have not been validated by three-dimensional imaging techniques. Following the same approach, other shapes like spherical or spheroidal shapes are potentially possible as well. Using the present 3D data set obtained by XRCT-imaging, we can investigate and identify the best fitting shape assumptions for the crystal aggregates.

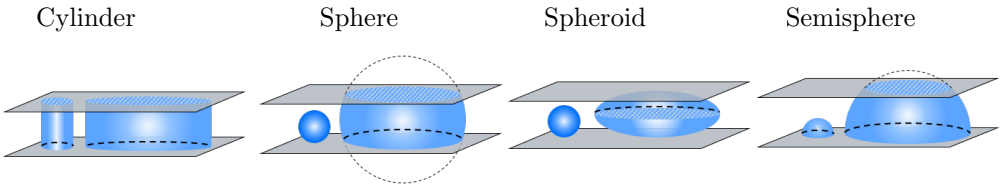

Figure 10. Hypothetical shape of crystal aggregates

$$V_{cylindrical} = \pi r_{eq}^2 H \tag{5a}$$

$$V_{semisphere} = \begin{cases} \frac{2}{3}\pi r_{eq}^3 & r_{eq} < H \\ \frac{\pi}{3}(3Hr_{eq}^2 - H^3) & r_{eq} > H \end{cases} \tag{5b}$$

$$V_{sphere} = \begin{cases} \frac{4}{3}\pi r_{eq}^3 & 2r_{eq} < H \\ \frac{\pi}{12}(12r_{eq}^2 H - H^3) & 2r_{eq} > H \end{cases} \tag{5c}$$

$$V_{spheroid} = \begin{cases} \frac{4}{3}\pi r_{eq}^3 & 2r_{eq} < H \\ \frac{2}{3}\pi r_{eq}^2 H & 2r_{eq} > H \end{cases} \tag{5d}$$

The following analysis is done using only the data gathered from XRCT-scans. Therefore, the projection of all planes from the XRCT-images are used as a hypothetical 2D image, since this corresponds to what could be observed by optical microscopy. Based on the projection the volumes are calculated assuming four different shapes respectively. Figure 11 shows the procedure for five crystals in the porous domain. The 2D projection of the XRCT-images is shown on the top. The original 3D structures of the five crystals are illustrated below in a). This is referred to as the reference. In b) the shapes are shown as spheroids as derived from the projected area, while c) shows the shapes assumed to be semi-spheres as proposed by Kim et al. (2020). In Figure 11, the volumes derived from the projected areas are plotted against the actual volume derived from the 3D data set, which is the reference volume. Therefore, the bisector, shown in black, corresponds to the perfect fitting of the volume derived from the projection and the reference volume. Each data point represents one crystal in the whole scanned domain. The assumption of a cylindrical shape clearly overestimates the volume of the crystal aggregates, which can be expected since the crystals do not fill the whole height of the micro-fluidic cell everywhere. The approaches of spherical and spheroidal shape are identical up to a volume of $0.32 \cdot 10^{-3}\text{mm}^3$, where the equivalent diameter is equal to the height of the cell. For larger aggregates, the spherical shape assumption also overestimates the volume, while the spheroidal approach is in good agreement to the reference volume. The semi-spherical approach mainly underestimates the volume of the crystals. Based on the coefficient of determination (R^2), it can be concluded that the spheroidal shape is the best choice in this case to determine the volume from a projected area.

Since our aim is to derive the volume from the images of optical microscopy, the final states of the crystal aggregates in the porous domain are analyzed and compared

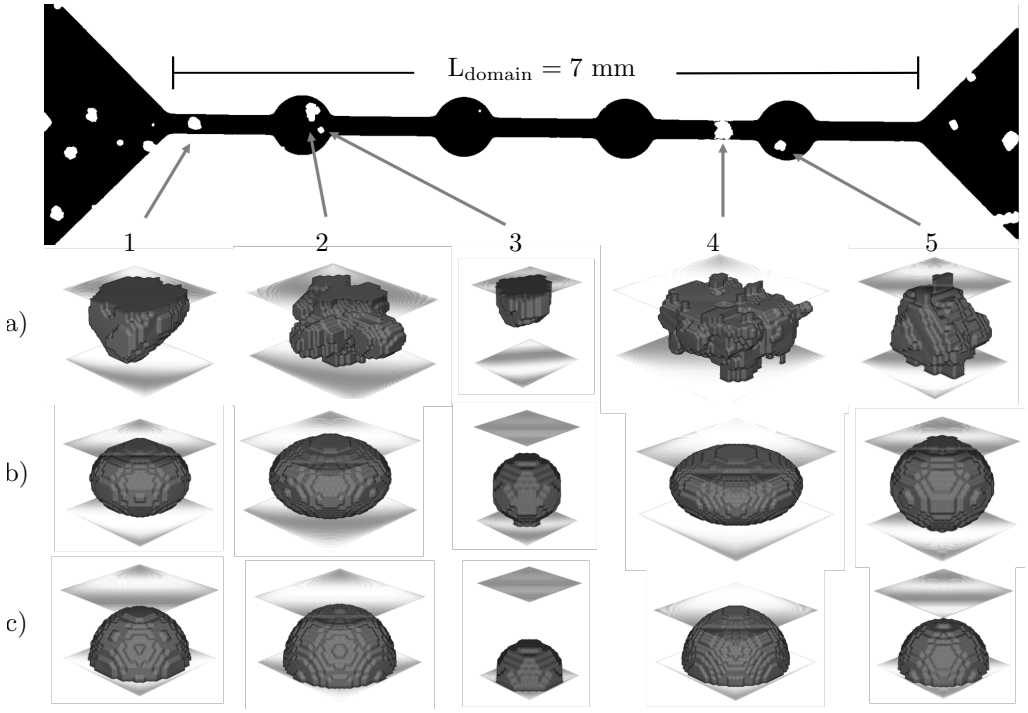

Figure 11. Shape of crystals: top) 2D projection (from XRCT-images) a) shape of crystals (from XRCT-scan); b) shape of crystals derived from 2D projection with the assumption of spheroidal shape; c) shape of crystals derived from 2D projection with the assumption of semi-spherical shape; the 3D representations of the crystals 1 - 5 are not exactly true to scale among each other.

to the XRCT-scan. In Table 3.3, the properties of five crystal aggregates in the porous domain are given, labeled corresponding to the labeling used in Figure 11. The projection area derived from the XRCT-scan, A_{XRCT}, differs slightly from the area observed by optical microscopy, $A_{optical}$. This is due to fact that these are two different imaging applications and, therefore, the post-processing has been done differently. Also, small changes that happened in the time period between the actual injection and precipitation experiment and the subsequent XRCT-scan may have caused small deviations. V_{XRCT} is the volume directly obtained from the XRCT-scan, as illustrated in Figure 11. The volume, derived from $A_{optical}$ assuming spheroidal shape slightly overestimates the volume. However, the averaged volume deviates by approximately 9 % and is therefore a good assumption to estimate the volume.

Based on this approach, the spheroidal shape is used to estimate the volume of the crystal aggregates from the images obtained by optical microscopy and to conclude on a change of porosity of the porous domain. Since the permeability can be calculated from the pressure data, we can relate the obtained average quantities, porosity and permeability, to each other. In the literature, there exist many different approaches of porosity-permeability relations which are used to model pore space alterations on the REV scale, like Kozeny-Carman type, Thullner Biofilm relation or Verma-Pruess type, to name only a few (Pandey et al., 2015; Thullner, 2010; Verma & Pruess, 1988). According to Hommel et al. (2018), many of them do not lead to fundamentally different permeability alterations compared to a simple power-law relation with a suitable exponent. In Figure 13, the decadic logarithm of the normalized permeability is plotted over the change of the porosity. The data set of Experiment 1 fits reasonably well to a power law with the ex-

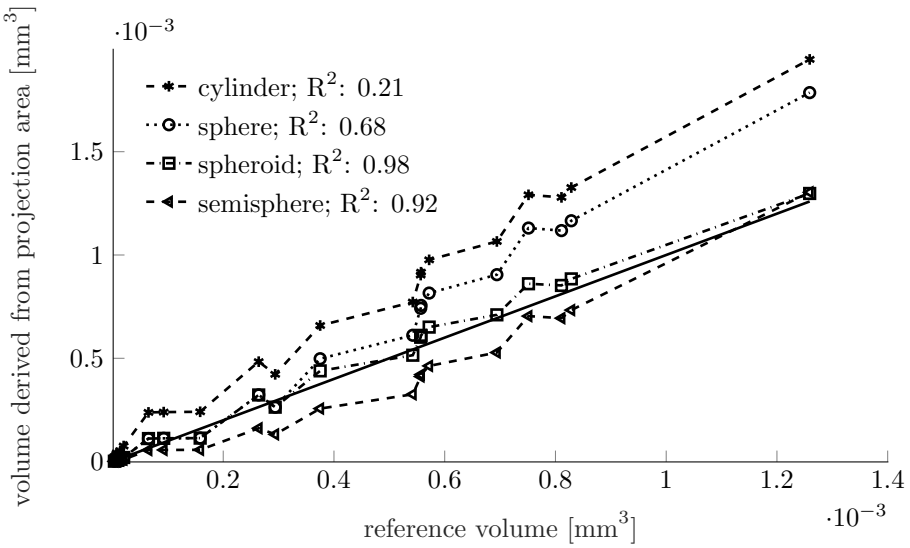

Figure 12. Volume derived from projection area of the XRCT-scan for different shape assumptions, including their coefficient of determination (R^2) with respect to the reference volume

Table 3. Comparison of estimated volumes from 2D images with the volume derived from XRCT-scans

Crystal	A_{XRCT} $[10^{-2}mm^2]$	$A_{optical}$ $[10^{-2}mm^2]$	V_{XRCT} $[10^{-3}mm^3]$	$V_{spheroid}$ $[10^{-3}mm^3]$
1	1.15	1.11	0.57	0.63
2	1.56	1.63	0.83	0.93
3	0.28	0.25	0.09	0.10
4	2.29	2.23	1.26	1.27
5	0.77	0.85	0.38	0.48
$\sum$	6.06	6.09	3.13	3.41

ponent 25. In contrast, Experiments 2 and 3 show a more sudden decrease of the permeability. While the decrease of permeability of Experiment 3 happens at a later point in time, it occurs at a lower porosity change. This effect underlines the hypothesis that if one single location is clogged, the permeability is decreased, even though the overall change of pore space is not significant. We can conclude from this that, at least for the specific geometry of our set-up, the location of the nuclei dominates the decrease of permeability rather than the averaged quantity porosity. Having in mind that the geometry chosen for the micro-fluidic cell only consists of four pore cavities connected with pore throats, it is far away from being a representative porous medium. Clogging of one single pore throat leads to a fast increase of the pressure drop and, therefore, to a decrease of the permeability. Discussing averaged quantities like permeability and porosity in this specific case does not have the aim of deriving or improving empirical relations yet, but to emphasize that the approach presented here offers a great possibility to tackle this topic when applying the set-up and procedures on more complex pore structures.

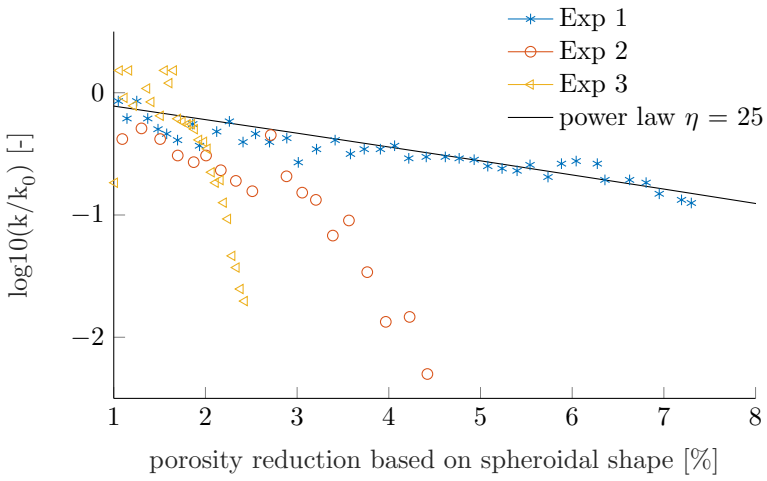

Figure 13. Decadic loagrithm of the relative permeability over porosity reduction for Experiment 1 - 3 and a power law relation with an exponent $\eta = 25$

4 Discussion

As explained in the Introduction, we consider this study to be in the context of finding specific porosity-permeability relationships for enzymatically induced calcite precipitation in porous media, and perspectively also for microbially induced calcite precipitation where biofilms additionally present in the pore space render the problem even more complex. As a porous medium we used flow cells made of PDMS, while we are aware of the possibility that the porous material and its surface may have an influence on the precipitation process, in particular on the generation of nucleation points due to locally increased roughness, surface charge, etc. This is definitely an aspect that we plan to consider in future studies.

What we have developed and presented above is an experimental strategy that we propose to assess pore-scale alteration observed during EICP in micro-fluidic cells. We note here that the main achievement of this study is the experimental procedure rather than results for the envisioned porosity-permeability relations. The requirements guiding us in designing the experimental procedure include a reliable determination of pore space alteration, which can be resolved also in time. In other words, our demand is to assess the when, where, and what are the processes taking place regarding precipitation during EICP with as much quantifiable data as possible. The cell design, the measurements, and the imaging techniques can be discussed in this context.

Regarding the design of the cell, we put an emphasis on a strongly simplified porous medium which allows for a detailed analysis of the shape of precipitated crystals. We note that this cell design due to its more-or-less 1D-like structure is not suited for deriving porosity-permeability relations in a representative porous medium. But the design is optimal for validating our workflow and it can, of course, be changed and adapted to required complexities in future studies. Another important aspect for the cell design is the evaluation of pressure at the desired locations, i.e. without being strongly influenced by precipitates in the inlet and outlet channels or tubes. With the designed pressure channels, we have found a satisfactory solution to this problem.

Evaluating the continuous pressure measurements during the three experiments, which we have presented in the Results section, we noted that they were increasingly reliable for increasing pressure drops. In the beginning of the experiments, or at low pres-

sure drops before significant precipitation occurred, we consider the pressure drops less reliable, they even showed values below zero in some instances, e.g. in Experiment 3 during 0.5 hours and 3 hours after start of injection. It might be caused by small leakage of fluid or other imperfections in the set-up. The continuous pressure measurements during injection and precipitation (Stage b) were necessary for the temporal resolution of the process. They were validated by permeability determination via injection of de-ionized water at varying rates both before the injection (and precipitation) and after its stop. This implies a small temporal shift due to the required changes in the set-up, during which precipitation in the cell may go on and further change the pore space and the permeability. Yet, we could see that this effect is minor and the "validation" of the continuous pressure monitoring can be considered successful.

While the pressure information is important for concluding on permeability changes, the imaging is the crucial part for the quantification of changes in pore morphology and pore volume. We have applied optical microscopy and as a subsequent 3D characterization technique XRCT scans. Similar to our approach with respect to the measurement of the pressure drop, we have here with the optical microscopy an approach of continuous monitoring during the injection and precipitation, while we use XRCT scans to prop up the more or less only 2D information from microscopy. Optical microscopy allows for observing changes of the pore structure synchronized with the continuous pressure measurements, but it does not resolve the structure of the precipitated solids in the third dimension. We have shown above, with the help of information from the XRCT scans, that the microscopy images can be usefully complemented by the approach of assuming spheroidal shapes. The XRCT scans, though costly and only a-posteriori to perform unless maybe at a synchroton tomography beamline, are able to resolve the third dimension. The shapes of the crystals can be examined and it enables finding of approximations for volumes derived from 2D projections, which, consequently, means that further on more value can be attributed to information from cheap and continuous optical microscopy. This combination of microscopy and XRCT scanning has thus proven very important for a better quantification of the changes in the pore space due to precipitation. However, the XRCT scans require preparations, the cells need to be flushed and then dried, moved to the scanner. Thus, it is likely that there occur some discrepancies between the "final" state of the injection/precipitation experiment and scanned state. Therefore, it is currently not practical to have time-resolved scanning during the experiment. This would require to apply for beam time in a synchroton. It is worth noting that the perfect experimental XRCT technique for a micro-fluidic cell, in which the aspect ratio of the depth to the other dimensions is small and is considered as flat, would be laminography (Gondrom et al., 1999). Nevertheless we were able to derive beneficial information out of the XRCT set-up, already available for us.

Another challenge we have encountered with the scanning is the occurrence of a second phase around the crystals. The existence of two phases can be due to the fact that although the cell is rinsed and dried directly after the experiment to keep the crystals as stable as possible, there is some remains of liquid in the cell which has a significantly different texture, despite coming across as parts of the crystal in the microscopy images. One may speculate that due to the existence of a big crystal in the pore throat, the cell is not rinsed and dried profoundly and trapped liquid including some chemicals have caused forming a second phase after the experiment, which could also be an outcome of the simple structure of the cell.

5 Conclusions

In this study, enzymatically induced calcite precipitation (EICP) is investigated in a micro-fluidic cell during a continuous injection of the reactive solutions. Three experiments were performed, all with the same boundary conditions. The design of the micro-fluidic cell allows for reliable continuous pressure measurements during the precipitation

and to obtain from them the permeability reduction of the porous domain. The domain in this study consists of four pore bodies connected with pore throats. Since the material of the cell is transparent, optical microscopy can be used to observe the growth of the crystal aggregates synchronized with the pressure measurements. We saw that most of the crystal aggregates stay at their position of initial nucleation and mainly grow into the upstream direction of the flow during the injection. However, in one experiment, we observed that a crystal in a pore body was transported with the flow into the next pore throat where it aggregated with another crystal. In addition to optical microscopy, XRCT-scans of one micro-fluidic cell after the precipitation process is performed in order to identify the best suited calculational shape for approximating the real shapes of the crystal aggregates from their 2D projection. The spheroidal shape has been found to approximate the volume best. Applying the assumption of a spheroidal shape, the volume of precipitates, and thus the change in pore volume, can then be derived based on the images from optical microscopy.

Thus, the averaged quantities porosity and permeability can be related to each other. In such a very simple porous domain as presented here, it was observed that the location of the precipitates, whether it occurs in the cavities or in the throats, dominates the evolution of the permeability rather than the total volume of the crystal aggregates.

The experimental procedure we proposed in this study can be applied for more realistic designs of the porous domain in two and three dimensions, where flow has more degrees of freedom to bypass clogging, in order to derive realistic porosity-permeability relations. These relations are crucially important when modeling reactive transport during EICP or MICP including precipitation on the REV scale. The method to derive the volume of the precipitates based on microscopy images can be applied in any kind of pore-structural design of the micro-fluidic cell.

The provided data include the segmented XRCT-scan, as well as the segmented images of microscopy. Based on these data, pore-scale simulations can be carried out.

Acknowledgments

The work was supported by the German Research Foundation (Deutsche Forschungsgemeinschaft, DFG) within the Collaborative Research Center 1313 (Project Number 327154368 – SFB 1313). We acknowledge funding by the DFG under Germany's Excellence Strategy EXC 2075 (Project Number 390740016 - EXC 2075). The datasets will be available in the data Repository of the University of Stuttgart (DaRUS). Two datasets are separately published: Images of optical microscopy together with the log data, including flow rates and pressure measurements, can be found in Weinhardt et al. (2020). The XRCT dataset is published in Vahid Dastjerdi et al. (2020).

The two datasets will be published along with the manuscript and are therefore not public yet. However, during the review process the datasets are accessible via the following url:

- Images of optical microscopy together with the log data:
  `https://darus.uni-stuttgart.de/privateurl.xhtml?token=594be1a3-8a5d-4dd1-bbb7-d405566edd41`
- XRCT dataset:
  `https://darus.uni-stuttgart.de/privateurl.xhtml?token=7b3a9da1-0399-47cd-b7c1-2ba478703532`

References

Bachmeier, K., Williams, A., Warmington, J., & Bang, S. (2012). Urease activity in microbiologically-induced calcite precipitation. *Journal of Biotechnology*, *93*, 171-181.

Cunningham, A., Class, H., Ebigbo, A., Gerlach, R., Phillips, A., & Hommel, J. (2019). Field-scale modeling of microbially induced calcite precipitation. *Computational Geosciences*, *23*, 399-414. doi: 10.1007/s10596-018-9797-6

Cuthbert, M., McMillan, L., Handley-Sidhu, S., Riley, M., Tobler, D., & Phoenix, V. (2013). A field and modeling study of fractured rock permeability reduction using microbially induced calcite precipitation. *Environmental Science & Technology*, *47*(23), 13637-13643. doi: 10.1021/es402601g

Ebigbo, A., Helmig, R., Cunningham, A., Class, H., & Gerlach, R. (2010). Modelling biofilm growth in the presence of carbon dioxide and water flow in the subsurface. *Advances in Water Resources*, *33*(7), 762-781. doi: 10.1016/j.advwatres.2010.04.004

Ebigbo, A., Phillips, A., Gerlach, R., Helmig, R., Cunningham, A., Class, H., & Spangler, L. (2012). Darcy-scale modeling of microbially induced carbonate mineral precipitation in sand columns. *Water Resources Research*, *48*(7), W07519. doi: 10.1029/2011WR011714

El-Sheikh, S., El-Sherbiny, S., Barhoum, A., & Deng, Y. (2013). Effects of cationic surfactant during the precipitation of calcium carbonate nanoparticles on their size, morphology, and other characteristics. *Colloids and Surfaces A Physicochemical and Engineering Aspects*, *422*, 44 - 49. doi: DOI:10.1016/j.colsurfa.2013.01.020

Gondrom, S., Zhou, J., Maisl, M., Reiter, H., Kröning, M., & Arnold, W. (1999). X-ray computed laminography: an approach of computed tomography for applications with limited access. *Nuclear Engineering and Design*, *190*, 141-147. doi: 10.1016/S0029-5493(98)00319-7

Hamdan, N., & Kavazanjian, E. (2016). Enzyme-induced carbonate mineral precipitation for fugitive dust control. *Géotechnique*, *66*(7), 546-555. doi: 10.1680/jgeot.15.P.168

Haubert, K., Drier, T., & Beebe, D. (2006). PDMS bonding by means of a portable, low-cost corona system. *Lab on a Chip*, *6*(12), 1548–1549. doi: 10.1039/b610567j

Hommel, J., Coltman, E., & Class, H. (2018). Porosity-permeability relations for evolving pore space: A review with a focus on (bio-)geochemically altered porous media. *Transport in Porous Media*, *124*, 589-629. doi: 10.1007/s11242-018-1086-2

Hommel, J., Cunningham, A., Helmig, R., Ebigbo, A., & Class, H. (2013). Numerical investigation of microbially induced calcite precipitation as a leakage mitigation technology. *Energy Procedia*, *40C*, 392-397. doi: 10.1016/j.egypro.2013.08.045

Hommel, J., Lauchnor, E., Gerlach, R., Cunningham, A., Ebigbo, A., Helmig, R., & Class, H. (2016). Investigating the influence of the initial biomass distribution and injection strategies on biofilm-mediated calcite precipitation in porous media. *Transport in Porous Media*, *114*(2), 557-579. doi: 10.1007/s11242-015-0617-3

Hommel, J., Lauchnor, E., Phillips, A., Gerlach, R., Cunningham, A., Helmig, R., ... Class, H. (2015). A revised model for microbially induced calcite precipitation: Improvements and new insights based on recent experiments. *Water Resources Research*, *51*(5), 3695-3715. doi: 10.1002/2014WR016503

Karadimitriou, N. K., Joekar-Niasar, V., Hassanizadeh, S. M., Kleingeld, P. J., & Pyrak-Nolte, L. J. (2012). A novel deep reactive ion etched (drie) glass micro-model for two-phase flow experiments. *Lab Chip*, *12*, 3413-3418. doi: 10.1039/C2LC40530J

Karadimitriou, N. K., Musterd, M., Kleingeld, P. J., Kreutzer, M. T., Hassanizadeh, S. M., & Joekar-Niasar, V. (2013). On the fabrication of pdms micromodels by rapid prototyping, and their use in two-phase flow studies. *Water Resources Research*, *49*(4), 2056-2067. doi: 10.1002/wrcr.20196

Kim, D. H., Mahabadi, N., Jang, J., & van Paassen, L. A. (2020). Assessing the kinetics and pore-scale characteristics of biological calcium carbonate precipitation in porous media using a microfluidic chip experiment. *Water Resources Research*, *56*(2), e2019WR025420. (e2019WR025420 2019WR025420) doi: 10.1029/2019WR025420

Kralj, D., Brečević, L., & Kontrec, J. (1997). Vaterite growth and dissolution in aqueous solution iii. kinetics of transformation. *Journal of Crystal Growth*, *177*(3), 248 - 257. doi: https://doi.org/10.1016/S0022-0248(96)01128-1

Kralj, D., Brečević, L., & Nielsen, A. E. (1990). Vaterite growth and dissolution in aqueous solution i. kinetics of dissolution. *Journal of Crystal Growth*, *104*(3), 793 - 800.

Kralj, D., Brečević, L., & Nielsen, A. E. (1994). Vaterite growth and dissolution in aqueous solution ii. kinetics of dissolution. *Journal of Crystal Growth*, *143*(3), 269 - 276.

Minto, J. M., Lunn, R. J., & El Mountassir, G. (2019). Development of a reactive transport model for field-scale simulation of microbially induced carbonate precipitation. *Water Resources Research*, *55*(8), 7229-7245. doi: 10.1029/2019WR025153

Mitchell, A. C., Espinosa-Ortiz, E. J., Parks, S. L., Phillips, A. J., Cunningham, A. B., & Gerlach, R. (2019). Kinetics of calcite precipitation by ureolytic bacteria under aerobic and anaerobic conditions. *Biogeosciences*, *16*(10), 2147–2161. doi: 10.5194/bg-16-2147-2019

Nebel, H. (2008). *Kontrollierte Fällung von CaCO3 in einem modular aufgebauten Kristallisationsreaktor* (Ph.D thesis). University of Duisburg-Essen, Essen.

Otsu, N. (1979). Threshold Selection Method From Gray-Level Histograms. *IEEE Trans Syst Man Cybern*, *SMC-9*(1), 62–66. doi: 10.1109/tsmc.1979.4310076

Pandey, S., Chaudhuri, A., Rajaram, H., & Kelkar, S. (2015). Fracture transmissivity evolution due to silica dissolution/precipitation during geothermal heat extraction. *Geothermics*, *57*, 111 - 126. doi: https://doi.org/10.1016/j.geothermics.2015.06.011

Perona, P., & Malik, J. (1990, July). Scale-space and edge detection using anisotropic diffusion. *IEEE Transactions on Pattern Analysis and Machine Intelligence*, *12*(7), 629–639. doi: 10.1109/34.56205

Phillips, A., Gerlach, R., Lauchnor, E., Mitchell, A., Cunningham, A., & Spangler, L. (2013). Engineered applications of ureolytic biomineralization: A review. *Biofouling*, *29*(6), 715-733. doi: 10.1080/08927014.2013.796550

Phillips, A., Lauchnor, E., Eldring, J., Esposito, R., Mitchell, A., Gerlach, R., ... Spangler, L. (2013). Potential CO_2 leakage reduction through biofilm-induced calcium carbonate precipitation. *Environmental Science & Technology*, *47*(1), 142-149. doi: 10.1021/es301294q

Ruf, M., & Steeb, H. (2020). An open, modular and flexible μXRCT system for research. *Review of Scientific Instruments*. (under review)

Thullner, M. (2010). Comparison of bioclogging effects in saturated porous media within one- and two-dimensional flow systems. *Ecological Engineering*, *36*(2), 176 - 196. (Special Issue: BioGeoCivil Engineering) doi: https://doi.org/10.1016/j.ecoleng.2008.12.037

Vahid Dastjerdi, S., Steeb, H., Ruf, M., Lee, D., Weinhardt, F., Karadimitriou, N., & Class, H. (2020). *micro-XRCT dataset of Enzymatically Induced Calcite Precipitation (EICP) in a micro-fluidic cell.* DaRUS. doi: 10.18419/darus-866

van Paassen, L. (2009). *Biogrout: Ground Improvement by Microbially Induced Carbonate Precipitation* (Ph.D. thesis). Delft University of Technology, Delft.

van Paassen, L., Ghose, R., van der Linden, T., van der Star, W., & van Loosdrecht, M. (2010). Quantifying biomediated ground improvement by ureolysis: large-scale biogrout experiment. *Journal of Geotechnical and Geoenvironmental Engineering*, *136*(12), 1721-1728. doi: 10.1061/(ASCE)GT.1943-5606.0000382

Verma, A., & Pruess, K. (1988). Thermohydrological conditions and silica redistribution near high-level nuclear wastes emplaced in saturated geological formations. *Journal of Geophysical Research: Solid Earth*, *93*(B2), 1159-1173. doi: 10.1029/JB093iB02p01159

Wang, Y., Soga, K., Dejong, J. T., & Kabla, A. J. (2019). A microfluidic chip and its use in characterising the particle-scale behaviour of microbial-induced calcium carbonate precipitation (micp). *Géotechnique*, *69*(12), 1086-1094. doi: 10.1680/jgeot.18.P.031

Weinhardt, F., Class, H., Vahid Dastjerdi, S., Karadimitriou, N., Lee, D., & Steeb, H. (2020). *Optical Microscopy and pressure measurements of Enzymatically Induced Calcite Precipitation (EICP) in a micro-fluidic cell.* DaRUS. doi: 10.18419/darus-818

Wiffin, V., van Paassen, L., & Harkes, M. (2007). Microbial carbonate precipitation as a soil improvement technique. *Geomicrobiology Journal*, *24*(5), 417-423. doi: 10.1080/01490450701436505

Xia, Y., & Whitesides, G. M. (1998). Soft lithography. *Angewandte Chemie International Edition*, *37*(5), 550-575. doi: 10.1002/(SICI)1521-3773(19980316)37:5⟨550::AID-ANIE550⟩3.0.CO;2-G

Yoon, H., Valocchi, A. J., Werth, C. J., & Dewers, T. (2012). Pore-scale simulation of mixing-induced calcium carbonate precipitation and dissolution in a microfluidic pore network. *Water Resources Research*, *48*(2), W02524. doi: 10.1029/2011WR011192

Zhang, C., Dehoff, K., Hess, N., Oostrom, M., Wietsma, T. W., Valocchi, A. J., ... Werth, C. J. (2010, Oct 15). Pore-scale study of transverse mixing induced caco3 precipitation and permeability reduction in a model subsurface sedimentary system. *Environmental Science & Technology*, *44*(20), 7833-7838. doi: 10.1021/es1019788

Supporting Information for "Experimental Methods and Imaging for Enzymatically Induced Calcite Precipitation in a micro-fluidic cell"

Felix Weinhardt[1], Holger Class[1], Samaneh Vahid Dastjerdi[2], Nikolaos Karadimitriou[2], Dongwon Lee[2], Holger Steeb[2,3]

[1]Department of Hydromechanics and Modelling of Hydrosystems, University of Stuttgart, Pfaffenwaldring 61, 70569 Stuttgart, Germany

[2]Institute of Applied Mechanics, University of Stuttgart,Pfaffenwaldring 7, 70569 Stuttgart, Germany

[3]SC SimTech, University of Stuttgart,Pfaffenwaldring 7, 70569 Stuttgart, Germany

Contents of this file Figures S1 to S4

Introduction

This supporting information provides two sketches of the experimental set-ups: one of the open and modular XRCT device (Figure S1) and another one of the custom made optical microscope, including the stage of the experimental set-up (Figure S2). Moreover, two flow charts describing the image processing steps are given: One visualizes the steps for the images taken by optical microscopy (Figure S3) and the other one for the XRCT dataset (Figure S5). Furthermore a comprehensive description of the image processing of the XRCT-dataset is given below.

Description of open and modular XRCT device

The scan was performed in open and modular XRCT device which was set-up during the last years. It is based on an open micro-focus tube with a tungsten transmission target (FineTec Force 180.01C TT, FineTec Technologies GmbH, Germany). The detector (Shad-o-Box 6K HS, Teledyne DALSA Inc., Waterloo, Ontario, Canada) has an active area of 146 $\times$ 114 mm^2 with a pixel size of 49.5 μm which results in images of the size of 2940 $\times$ 2304 pixels. The Shad-O-Box detector has a CsI-scintillator and the image output of the detector is realized via GigE interfaces using LAN connections to the computer. The cone-beam scanning process was carried out without any physical filtering. A schematic illustration of the scanning device can be seen in S1. The voltage, the current, and the exposure time were set to 80 kV, 100 μA and 3000 ms respectively. The scan consists of 1800 projections (5 rotation fragments per degree). In order to minimize ring artefacts, the output of 5 slightly shifted projections are averaged at each (rotational) position. Therefore, the detector was moved slightly to the left, right, up, and down. The resolution was set to 4.25 $^{\mu m}/_{px}$ to obtain 20 voxels in the depth of the porous domain. Given the total number of 9005 images, the scanning has taken 15 hours and 46 minutes. Reconstruction of the 3D volume is performed by the software tool Octopus Reconstruction (Version 8.9.4-64 bit). A schematic illustration of the set-up is shown in Figure S1.

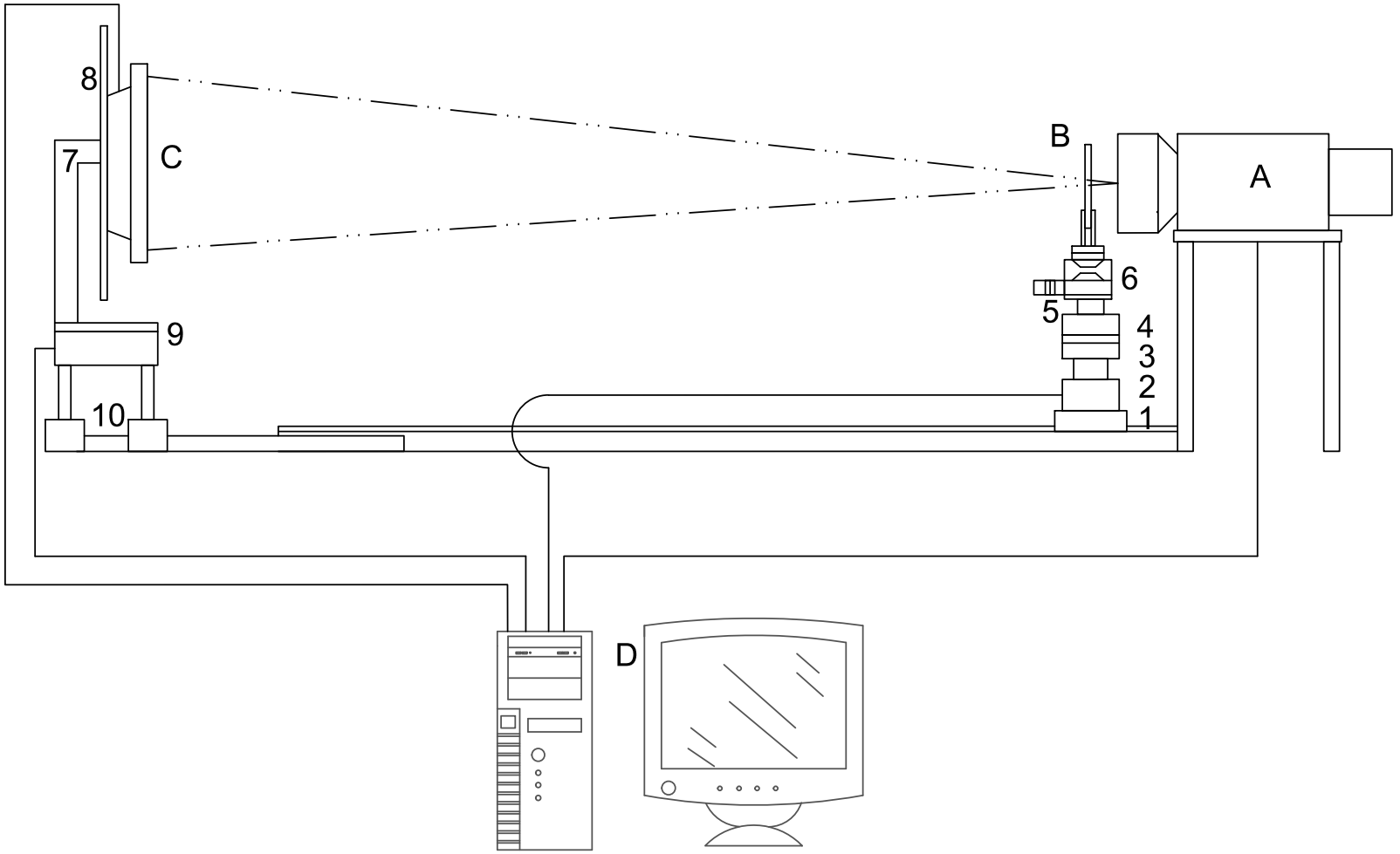

Figure S1. Components of the open and modular XRCT device: (A) shows the micro-focus source. (B) is the cell under XRCT investigation. Further, various (motorized) stepper and DC motor-based stages (1-6) including the rotational stage (4) and various translation stages (1-3) and the x-y-stages (5-6) for sample positioning are shown. (C) is the detector and the stages (8-10) are used for detector movements incl. ring artefact minimization. The stages, the detector and the source are computer-controlled (D) with in-house tools

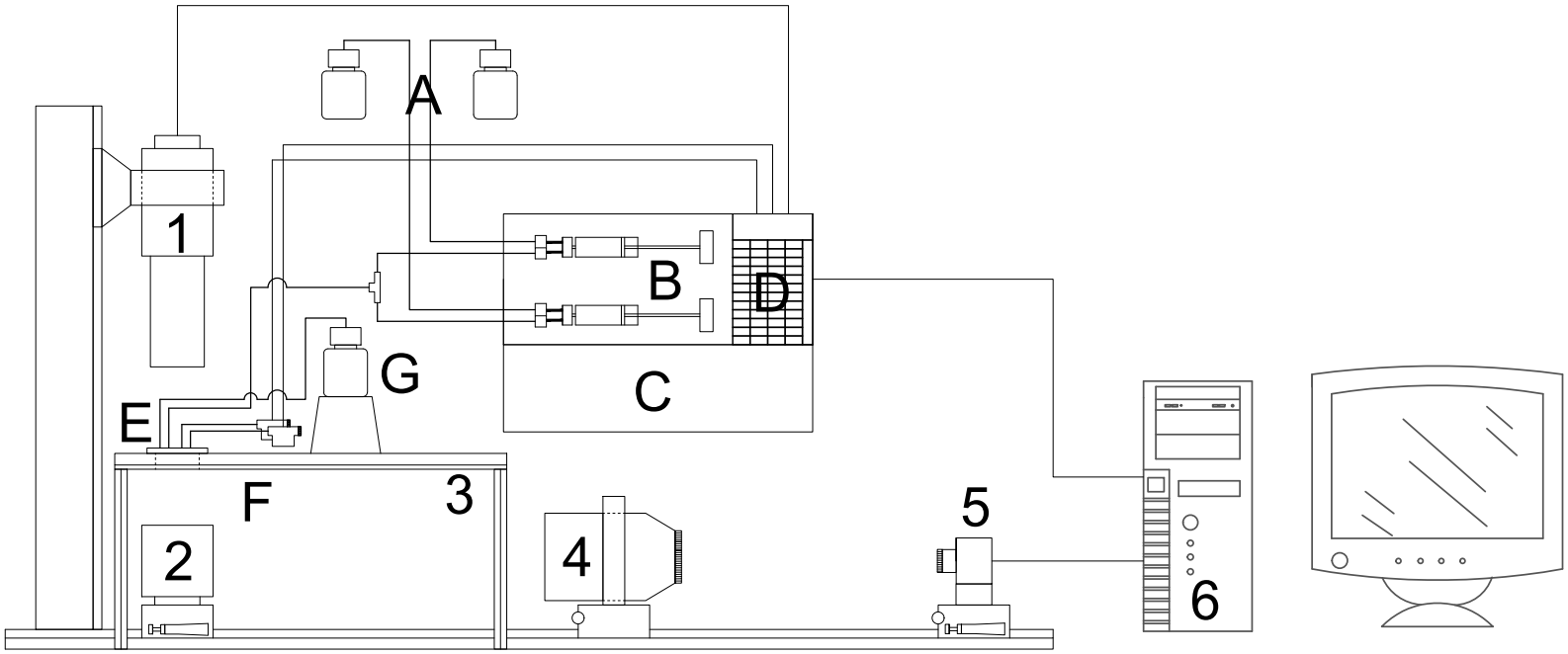

Figure S2. 1-6: Parts of the open microscope; 1: Light source (1W LED light source emitting at 590 nm mounted on Canon objective lens with F 3.2/135 mm); 2: Prism (Edmund Optics with dimension of 50 mm x 50 mm); 3: Stage for the micro-fluidic cell; 4: Lens (Sigma 135 mm F1.8 DG HSM telephoto lens); 5: Camera (Allied Vision GigE GC-D-2450 camera with a 5 Mpx sensor); 6: Computer. A-G: Parts of the micro-fluidic system: A: Reservoir (filled with water for stage a and c or filled with the two reactive solutions for stage b; B: Syringe pumps (CETONI neMESYS 100N) C: CETONI base module; D: CETONI I/O module 16 bit; E: micro-fluidic cell; F: Pressure sensors (Elveflow MPS03, range 0 – 70 mbar); G: Outlet reservoir

Detailled description of image processing for the XRCT-dataset

In Figure S5 various stages of the image processing, carried out to extract the desired data out of the reconstructed images from the XRCT. Embedded in the process, which is already explained in the paper, there are some measures, taken to tackle the existence of a second phase around some of the crystals. In the following, the mentioned processes are described.

After the 3D dataset was cutted and aligned, it was read into Matlab R2019b (The Mathworks, Inc.) as 20 images, each representing one layer in the depth of the channel. Then images were segmented using the "Max Entropy Thresholding" method. This method gave us the precipitates along with parts of the channel wall. So, there was a need for a mask to remove the non-relevant voxels. By adding up all the segmented images together, and cleaning the resulting image manually, a mask was prepared. This was done to avoid cleaning all of the images one by one. This mask was multiplied by all of the images to remove the noise but keep the crystals untouched. In another attempt, the same procedure was carried out with one difference: The segmentation was done by multithresholding, Otsu's method. This gave us the crystals which has some other phase around them, in two parts. The reason why the multithresholding, Otsu's method is not used for all of the crystals, is that a layer around the crystals have the same gray value as in the second phase and is categorized as the second phase. To sum it up, 4 of the crystals where a second phase is observed in the XRCT were segmented with multithresholding, Otsu method and the rest with maximum entropy. There was an issue with the multi-thresholding method, which needed to be addressed: Due the gray value distribution on the first and last slide, this method, classifies all of the voxels on the top and at the bottom of the channel as the second phase. That led for the crystals, with the second phase around them to be connected to nowhere, which is physically not possible. For this reason a closer look at the not processed XRCT images

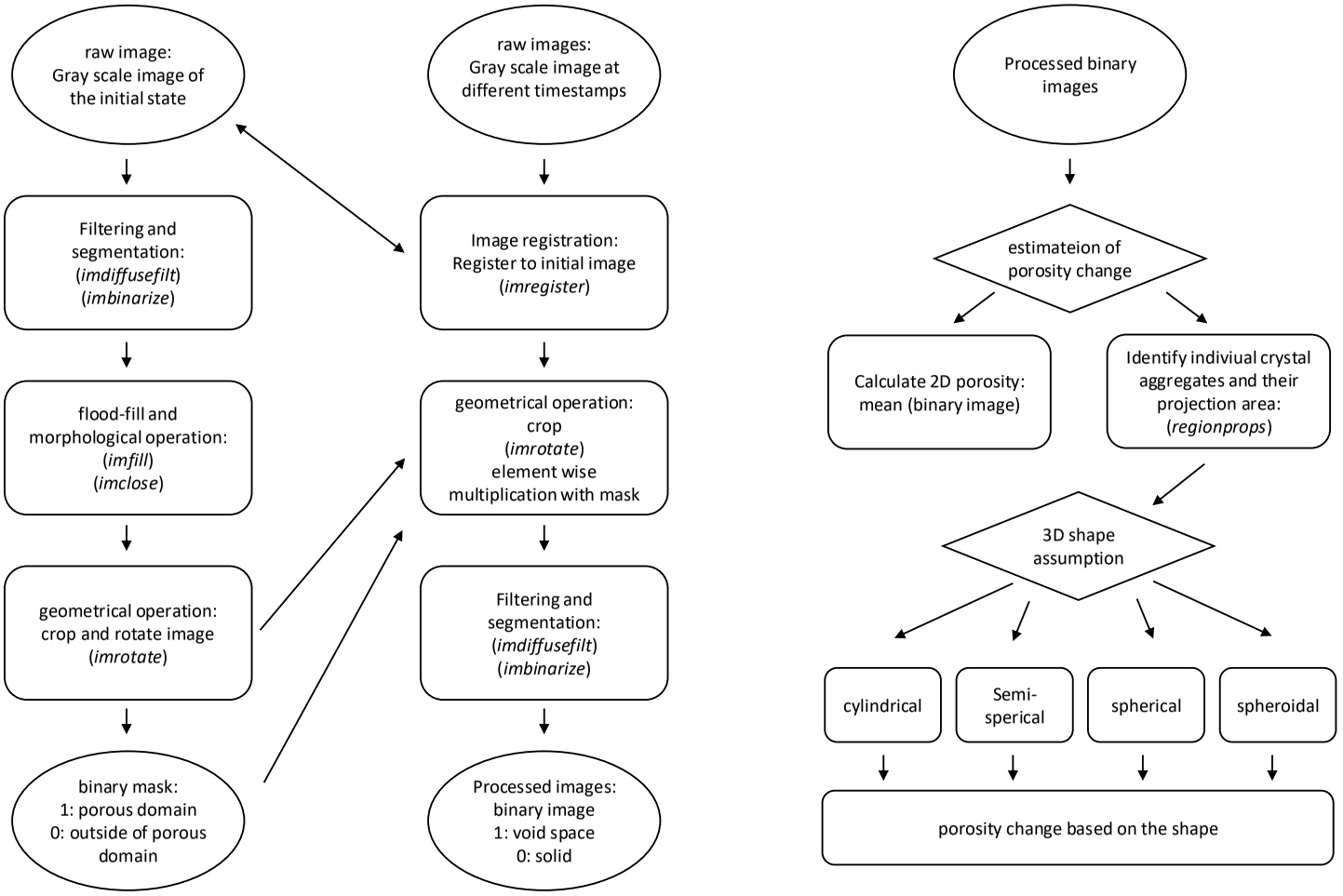

Figure S3. Flow chart of image processing for optical microscopy images. Left: Creating the mask from the initial image; mid: segmenting the gray scale images; right: further processing of the segmented images in order to calculate the pore space ration of the precipitates

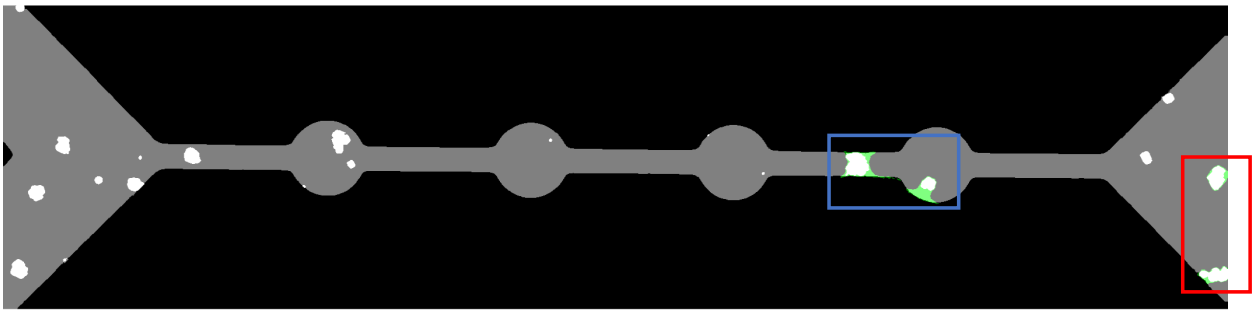

Figure S4. Second phase allocation in the precipitated cell

was required to have a dataset resembling the XRCT as good as possible. The XRCT-images guided us to the following:

The four crystals marked with the blue and red box in S4 are the crystals with the second phase around them. However they are not treated similarly and that is because a bow form is observed in the channel, meaning that the channel is not completely horizontal. The middle of the channel is roughly 2 voxels higher than the two ends. The 20 slides which are defining the channel depth are chosen with reference to the middle of the cell. For the two crystals which are in the middle of the cell and are not affected by the hypothetically physically bow form of the channel (marked with the blue box), the following is done: The last layer of the crystal in depth is defined as the layer below it. It means in the final dataset, the 1^{st} and 20^{th} layer of these two crystals is the same as the 2^{nd} and 19^{th} respectively. For the other two (marked with red box) which are placed closed to the edges, other measures are carried out. In them the crystals are shifted three voxels up and the first three layers are defined as the fourth one. It means that the 1^{st}, 2^{nd} and 3^{rd} layers of the named crystal, resemble the 4^{th} one. Finally the segmented volume of the all of the crystals were put together as the final dataset and used for the investigations.

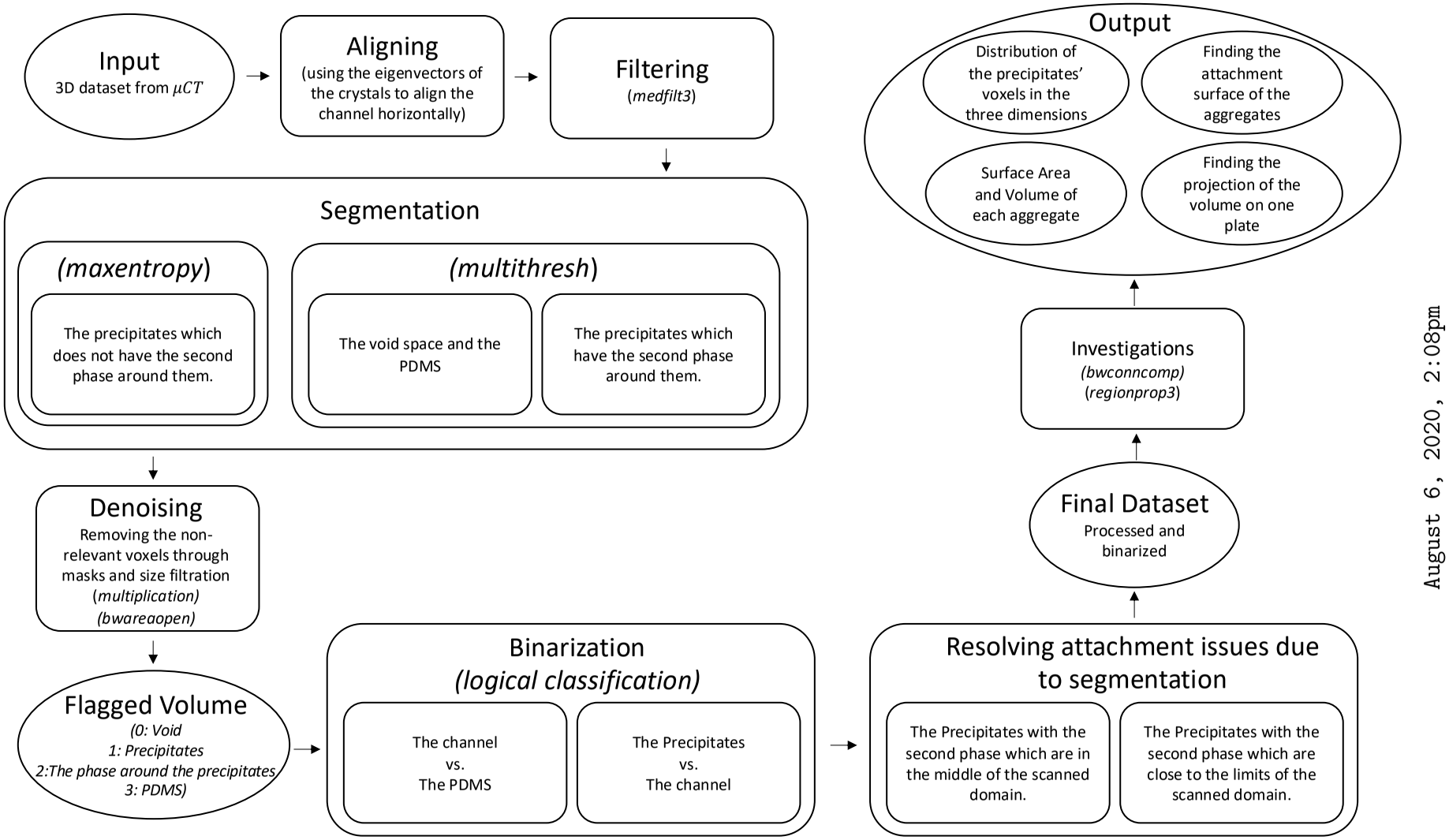

Figure S5. Flow chart of image processing for XRCT images.